Strain effect analysis on phonon thermal conductivity of two-dimensional nanocomposites

Y. Xu and G. Li[a)]
Department of Mechanical Engineering, Clemson University, Clemson, South Carolina 29634-0921, USA

(Received 2 June 2009; accepted 10 October 2009; published online 1 December 2009)

In this paper, we present a model that combines lattice dynamics and the phonon Boltzmann transport equation (BTE) to analyze strain effect on the cross-plane phonon thermal conductivity of silicon wire-germanium host nanocomposites. For a given strain condition, mechanical strain is translated to crystal lattice deformation by using the Cauchy–Born rule. Strain-dependent phonon thermal properties of Si and Ge obtained from lattice dynamics with Tersoff empirical interatomic potential are then incorporated into the BTE, in which ballistic transport within one material and diffuse scattering between Si–Ge interface are employed. The strain-dependent BTE is solved numerically on an unstructured triangular mesh by using a finite volume method. Nanocomposites with different Si nanowire cross sections are also investigated. The results show that the phonon thermal conductivity of the nanocomposites can be significantly decreased (or increased) by a tensile (or compressive) strain. With the same length change, hydrostatic strain produces a larger variation in phonon thermal conductivity than uniaxial strain. In addition, it is shown that with the same atomic percentage, the cross-sectional shape makes little difference to the thermal conductivity except at very small characteristic lengths of the Si nanowire. © *2009 American Institute of Physics*. [doi:10.1063/1.3259383]

I. INTRODUCTION

In the past decade, synthesis and processing techniques have been developed to create nanostructured materials with highly controlled material composition, structures, and related physical properties.[1–4] Examples of the engineered nanostructures include nanotubes, quantum dots, superlattices, thin films, and nanocomposites. For these nanostructured solids, thermal conductivity is one of the most important physical properties. Manipulation and control of thermal conductivity in nanostructured materials such as nanocomposites have impacted a variety of applications. A well-known example is the enhancement in energy conversion efficiency in thermoelectric devices,[5] which is measured by the dimensionless figure of merit $ZT=S^2\sigma T/k$, where T is the temperature, S is the Seebeck coefficient, σ is the electrical conductivity, and k is the thermal conductivity, which includes the contribution from phonon thermal conductivity and electronic thermal conductivity.[6] It has been shown that the phonon thermal conductivity can be reduced significantly in nanocomposites due to the increase in phonon interface scattering, while the electron performance can be maintained or improved.[7,8] Significant increases in ZT values with nanocomposites have been reported.[9,10] A few other applications utilize nanocomposites to enhance thermal conductivity, such as packaging materials of microelectronic circuits and chips[11] and conducting polymer nanocomposites.[12] While the size and volume fraction effects on the thermal conductivity of nanocomposites have been investigated using computational analysis techniques,[13] strain effect, which falls in a broader category of mechanical effects, has not attracted much attention in the design of nanocomposite materials. Computational analysis of strain effect on the phonon thermal conductivity could introduce additional dimensions to the design space of nanocomposites for various applications.

Thermal conductivity of doped semiconductors under uniaxial stress at low temperatures is relatively well-understood.[14–17] Recently, residual strain in nanocomposite materials has been studied by several groups. Borca-Tasciuc *et al.*[18] measured thermal conductivity in the cross-plane direction of symmetrically strained Si–Ge superlattices. Abramson *et al.*[19] studied interfacial strain on phonon transport and thermal conductivity of heterostructures around Debye temperature by molecular dynamics (MD) study. Picu *et al.*[20] have also employed MD to study the residual strain effect on heat transport in nanostructures by using a Lennard-Jones solid at low temperatures and concluded that tensile (or compressive) strain led to a reduction (or enhancement) in the lattice thermal conductivity. While these studies have shown the significance of strain on the nanoscale thermal transport, they are limited to single crystal materials or the residual strain effect at the interface of two different materials. Thermal conductivity variation in nanocomposite materials due to externally applied mechanical strain has not been studied. In addition, either analytical or pure atomistic methods such as MD were employed in previous studies of strain effect. In strained nanocomposites, it is difficult to study the strain effect by using analytical approaches due to multiple material phases and complex geometry of the inclusion phase. Although lattice strain can be accommodated in MD calculations, the size of the system is limited due to the computational cost. For nanocomposites with characteristic length larger than a few nanometers, MD simulations would become very inefficient. Another nano-

a)Author to whom correspondence should be addressed. Electronic mail: gli@clemson.edu.

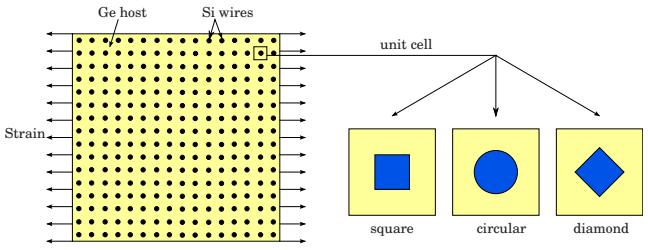

FIG. 1. (Color online) $Si_{0.2}Ge_{0.8}$ nanocomposite material with applied strain.

scale thermal transport analysis approach is based on the Boltzmann transport equation (BTE).[21] This approach provides greater computational flexibility and efficiency. It has been successfully applied to compute the effective thermal conductivity of complex materials including nanocomposites.[13] However, this approach does not include mechanical variables such as strain in the model.

In this paper, we present an approach that enables the calculation of thermal conductivity of strained nanocomposite materials. The main idea is combining the lattice dynamics for phonon dispersion change (i.e., wave effects) due to strain with the BTE for interface scattering of phonons (i.e., particle effects). Several strain-dependent phonon scattering properties of the materials are used to link the lattice dynamics and the BTE. In this approach, there is no fitting parameter in the calculation. In addition, the finite-volume solution of BTE over unstructured meshes allows thermal transport analysis of nanocomposites with complex geometries. In this work, we focus on the calculation of the cross-plane thermal conductivity of a $Si_{0.2}Ge_{0.8}$ composite with silicon wires embedded in germanium host under tensile and compressive hydrostatic and uniaxial strain conditions, as depicted in Fig. 1. For comparison, the thermal conductivity variation in Si–Ge composites corresponding to square, circular and diamond Silicon wire cross sections is calculated.

This paper is organized as follows: Sec. II presents the theoretical model and computational procedure, including lattice dynamics approach for computing the strain-dependent phonon scattering properties and the finite-volume solution of BTE for the nanocomposites. Results are shown and discussed in Sec. III, and Sec. IV gives the conclusions.

II. THEORETICAL MODEL AND COMPUTATIONAL PROCEDURE

Figure 2 illustrates the theoretical model of the analysis. In this approach, atomic interactions are described by using interatomic potentials. Mechanical strains are translated to crystal lattice deformation by applying the Cauchy–Born rule. For the deformed crystal lattice, we employ the lattice dynamics theory to compute the strain-dependent phonon scattering properties for both silicon and germanium, including the group velocity, specific heat, and phonon mean free path (MFP). The strain-dependent phonon scattering properties are then incorporated into the BTE to describe the thermal transport with interface scattering in the strained nanocomposites. Along with the BTE, a diffuse mismatch model is adopted for the Si–Ge interface. In the numerical solution of BTE, a unit cell of the nanocomposite material is taken as the computational domain with a periodic boundary condition. The unit cell is discretized into unstructured triangular volumes. The BTE is solved over the unstructured mesh by using a finite-volume formulation. Heat flux and effective temperature are calculated for the volumes and faces from the intensity solution of the BTE. The strain-dependent effective thermal conductivity can then be obtained.

Several assumptions are implied in the theoretical model described above: (1) Strain is assumed to be uniformly distributed throughout the nanocomposites, and residual strain is not considered between Si–Ge interfaces; (2) the BTE model employs a "gray" assumption with a single group velocity and single relaxation time;[22] (3) three-phonon scattering dominates the thermal transport within each material, and phonon scattering due to defects and/or impurities is neglected; and (4) the scattering between Si–Ge interface is assumed to be diffuse.

A. Strain-dependent lattice dynamics

At the atomistic level, interaction between atoms in diamond crystal lattices can be described by empirical interatomic potentials such as the Tersoff,[23] Brenner,[24] and Stillinger–Weber[25] potentials. Tersoff empirical interatomic potential is employed in this work for Si and Ge. Typically, the total potential energy U of a N atom system is given by

$$U = \sum_{\alpha} U_{\alpha} = \frac{1}{2} \sum_{\alpha \neq \beta} V_{\alpha\beta}, \tag{1}$$

where α and β are the atoms of the system and $V_{\alpha\beta}$ is the bond energy between atoms α and β given by

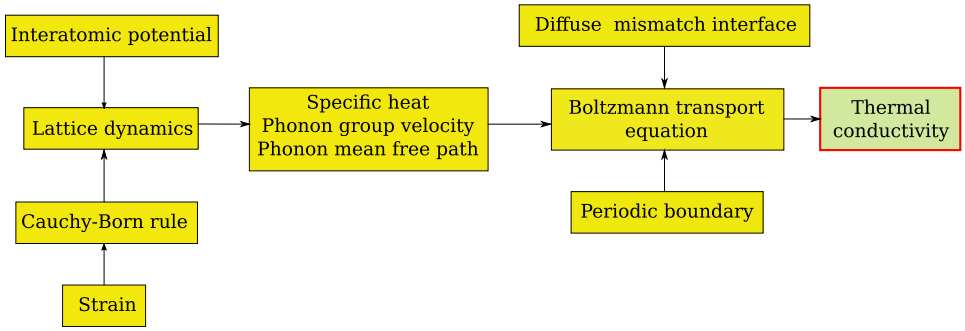

FIG. 2. (Color online) Theoretical model of the analysis.

$$V_{\alpha\beta} = f_C(r_{\alpha\beta})[a_{\alpha\beta} f_R(r_{\alpha\beta}) + b_{\alpha\beta} f_A(r_{\alpha\beta})], \tag{2}$$

where $r_{\alpha\beta}$ is the distance between α and β, f_R and f_A denote the repulsive and attractive pair potentials defined as

$$f_R(r) = Ae^{-\lambda_1 r}, \tag{3}$$

$$f_A(r) = -Be^{-\lambda_2 r}, \tag{4}$$

respectively, and $f_C(r_{\alpha\beta})$ is a smooth cutoff function going from 1 to 0 in a small range around the cutoff distance R_c, which is chosen to include only the first-neighbor shell for most structures of interest. $f_C(r)$ is defined as

$$f_C(r) = \begin{cases} 1 & r < R_c - D \\ \frac{1}{2} - \frac{1}{2}\sin\left[\frac{\pi(r - R_c)}{2D}\right] & R_c - D \le r \le R_c + D \\ 0 & r > R_c + D \end{cases}. \tag{5}$$

In Eq. (2), $a_{\alpha\beta}$ is taken to be 1.0 for both silicon and germanium, $b_{\alpha\beta}$ is a measure of the bond order given by

$$b_{\alpha\beta} = (1 + \mu^n \zeta_{\alpha\beta}^n)^{-1/2n}, \tag{6}$$

$$\zeta_{\alpha\beta} = \sum_{\kappa \neq \alpha,\beta} f_C(r_{\alpha\kappa}) g(\theta_{\alpha\beta\kappa}) \exp[\lambda_3^3 (r_{\alpha\beta} - r_{\alpha\kappa})^3], \tag{7}$$

$$g(\theta_{\alpha\beta\kappa}) = 1 + c^2/d^2 - c^2/[d^2 + (h - \cos\ \theta_{\alpha\beta\kappa})^2], \tag{8}$$

where κ denotes an atom and $\theta_{\alpha\beta\kappa}$ is the bond angle between the bonds $\alpha\beta$ and $\alpha\kappa$. All remaining variables are constant parameters. For silicon, the constants are summarized in the third column of Table I in Ref. 23. For germanium, the constants are adopted from Table I in Ref. 26.

In the classical lattice dynamics, by using the periodicity of the crystal structure, the phonon frequency spectrum can be obtained by computing the eigenvalues of the dynamical matrix $\mathbf{D}(\mathbf{k})$ for each wave vector $\mathbf{k}$ in the first Brillouin zone, i.e.,[27]

$$\mathbf{D}(\mathbf{k}) = \frac{1}{M}\begin{bmatrix} \sum_\beta \Phi_{j,k}^{11}(\alpha,\beta) e^{i\mathbf{k}\cdot(\mathbf{x}_\beta^0 - \mathbf{x}_\alpha^0)} & \sum_\beta \Phi_{j,k}^{12}(\alpha,\beta) e^{i\mathbf{k}\cdot(\mathbf{x}_\beta^0 - \mathbf{x}_\alpha^0)} \\ \sum_\beta \Phi_{j,k}^{21}(\alpha,\beta) e^{i\mathbf{k}\cdot(\mathbf{x}_\beta^0 - \mathbf{x}_\alpha^0)} & \sum_\beta \Phi_{j,k}^{22}(\alpha,\beta) e^{i\mathbf{k}\cdot(\mathbf{x}_\beta^0 - \mathbf{x}_\alpha^0)} \end{bmatrix} \quad j,k = 1,2,3, \tag{9}$$

where α and β denote the atoms in the unit cell, M is the mass of atom, $\mathbf{k}$ is wave vector, $\mathbf{x}_\alpha^0$ and $\mathbf{x}_\beta^0$ are the equilibrium positions of atom α and β, respectively, and $\Phi_{j,k}^{pq}(\alpha,\beta)$ is force constant defined by

$$\Phi_{j,k}^{pq}(\alpha,\beta) = \left.\frac{\partial^2 U(\mathbf{x})}{\partial \mathbf{x}_{\alpha j}\, \partial \mathbf{x}_{\beta k}}\right|_{\mathbf{x}=\mathbf{x}^0, \alpha \in B_p, \beta \in B_q} \quad j,k = 1,2,3 \quad p,q = 1,2, \tag{10}$$

in which $\mathbf{x}_{\alpha j}$ and $\mathbf{x}_{\beta k}$ are the jth and the kth component of the position of atoms α and β, respectively. B_p and B_q are Bravais lattices p and q, respectively. Note that we choose α to be the center atom and loop atom β over all the atoms in the crystal lattice. The phonon frequencies can be calculated by $\omega_{s\mathbf{k}} = \sqrt{\lambda_{s\mathbf{k}}}$, where $\lambda_{s\mathbf{k}}$ are the eigenvalues of the 6×6 dynamical matrix $\mathbf{D}(\mathbf{k})$ and s is the index of the polarization.

When there is an applied strain, to relate the continuum level description of deformation to displacements of the atoms in the crystal lattice as shown in Fig. 3, we employ the hypotheses of the Cauchy–Born rule,[28] which states that the crystal lattice is homogeneously distorted according to the deformation gradient. For silicon/germanium crystal, there exist additional inner displacements between the two Bravais lattices. The Cauchy–Born rule gives

$$\mathbf{x}_\beta^0 - \mathbf{x}_\alpha^0 = \mathbf{F}(\mathbf{X}_\beta^0 - \mathbf{X}_\alpha^0) + \boldsymbol{\xi}, \tag{11}$$

where $\mathbf{F}$ is the deformation gradient of the Bravais lattice, $\mathbf{X}_\alpha^0$ and $\mathbf{X}_\beta^0$ are the equilibrium positions of atom α and β in the undeformed configuration, respectively, and $\boldsymbol{\xi}$ is the inner displacement of the two fcc Bravais lattices. In the reciprocal lattice of a Bravais lattice, from Eq. (11), it is easy to show that, a given wave vector $\mathbf{k}^0$ in the undeformed configuration of the lattice deforms to $\mathbf{k}$ in the deformed configuration with the relation

$$\mathbf{k} = \mathbf{F}^{-T}\mathbf{k}^0. \tag{12}$$

Substituting Eqs. (11) and (12) into Eq. (9), the strain-dependent dynamical matrix can then be written as[27]

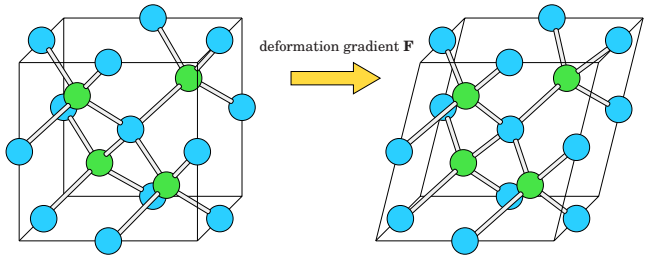

FIG. 3. (Color online) Atom configuration and deformation for a diamond lattice.

$$\mathbf{D}(\mathbf{k}) = \frac{1}{M}\begin{bmatrix} \sum_{\beta} \bar{\Phi}_{jk}^{11}(\alpha,\beta) e^{i\mathbf{k}^0\cdot(\mathbf{X}_\beta^0 - \mathbf{X}_\alpha^0)} & \sum_{\beta} \bar{\Phi}_{jk}^{12}(\alpha,\beta) e^{i\mathbf{k}^0\cdot(\mathbf{X}_\beta^0 - \mathbf{X}_\alpha^0 - \mathbf{F}^{-1}\boldsymbol{\xi})} \\ \sum_{\beta} \bar{\Phi}_{jk}^{21}(\alpha,\beta) e^{i\mathbf{k}^0\cdot(\mathbf{X}_\beta^0 - \mathbf{X}_\alpha^0 + \mathbf{F}^{-1}\boldsymbol{\xi})} & \sum_{\beta} \bar{\Phi}_{jk}^{22}(\alpha,\beta) e^{i\mathbf{k}^0\cdot(\mathbf{X}_\beta^0 - \mathbf{X}_\alpha^0)} \end{bmatrix} \quad \alpha = 1, \quad j,k = 1,2,3, \tag{13}$$

where

$$\bar{\Phi}_{j,k}^{pq}(\alpha,\beta) = \left.\frac{\partial^2 U(\mathbf{x})}{\partial \mathbf{x}_{\alpha j}\, \partial \mathbf{x}_{\beta k}}\right|_{\mathbf{x}=\mathbf{x}^0(\mathbf{X}^0,\mathbf{F},\boldsymbol{\xi}),\alpha\in B_p,\beta\in B_q} \quad j,k = 1,2,3 \quad p,q = 1,2 \tag{14}$$

and $\mathbf{F}^{-1}$ is the inverse of $\mathbf{F}$. The phonon frequencies of the strained bulk crystal Si and Ge, $\omega_{s\mathbf{k}}(\mathbf{F},\boldsymbol{\xi})$, can be obtained by computing the eigenvalues of Eq. (13). After the phonon frequency spectrum is obtained, the Helmholtz free energy A of the system can be calculated by

$$A = U(\mathbf{X}^0,\mathbf{F},\boldsymbol{\xi}) + \frac{1}{2}\sum_{\mathbf{k}}\sum_{s=1}^{6} \hbar\omega_{s\mathbf{k}}(\mathbf{F},\boldsymbol{\xi}) + k_B T \sum_{\mathbf{k}}\sum_{s=1}^{6} \ln[1 - e^{-\hbar\omega_{s\mathbf{k}}(\mathbf{F},\boldsymbol{\xi})/k_B T}], \tag{15}$$

where $U(\mathbf{X}^0,\mathbf{F},\boldsymbol{\xi})$ is the total potential energy of the system at the deformed equilibrium position, $\hbar$ is the reduced Planck's constant, k_B is the Boltzmann constant, and T is temperature. For a given deformation gradient $\mathbf{F}$, the inner displacement $\boldsymbol{\xi}$ can be determined by minimizing the Helmholtz free energy, i.e.,

$$\frac{\partial A}{\partial \boldsymbol{\xi}} = 0. \tag{16}$$

In this work, we impose uniaxial strains from −2% (compressive) to 2% (tensile) in the x-direction, which gives a maximum of 2% change in the crystal volume. This range of the strain is achievable with moderate external loadings. In terms of the deformation gradient, the uniaxial strains correspond to $F_{11}=[0.98,1.02]$, $F_{22}=F_{33}=1.0$, and $F_{ij}=0$, $i\neq j$. For the hydrostatic strains, $F_{ii}=[0.98,\ 1.02]$, $i=1,2,3$ and $F_{ij}=0$, $i\neq j$. Note that for hydrostatic and uniaxial deformations, $\boldsymbol{\xi}=0$ due to the symmetry of the lattice deformation.

B. Strain-dependent thermodynamic and phonon scattering properties

For a given deformation gradient $\mathbf{F}$, we compute the phonon frequency spectrum of Si and Ge lattices by sampling the $\mathbf{k}$ points in the first Brillouin zone. Once the phonon frequency spectrum is obtained, the bulk thermodynamic and phonon scattering properties of Si and Ge can be calculated. Of particular interest are the specific heat, the average phonon group velocity, and the average phonon MFP. As will be described in Sec. II C, they are the physical variables used in the BTE for the analysis of thermal transport in the Si–Ge nanocomposites. To compute these thermodynamic and phonon scattering properties, we first compute the bulk thermal conductivity of Si and Ge as a function of $\mathbf{F}$ by using the Slack relation.[29,30] The Slack relation is suitable for calculating the thermal conductivity of nonmetallic crystals at high temperatures (above 1/5 of the Debye temperature), where heat is mainly carried by acoustic phonons and the scattering is mainly intrinsic three-phonon process. The bulk thermal conductivity is given by[29,30]

$$k_b = \frac{3.1\times 10^7 \langle M\rangle \delta T_D^3}{T\langle\gamma^2\rangle N_c^{2/3}}, \tag{17}$$

where $\langle M\rangle$ is the average atomic mass of the crystal, δ^3 is the average volume per atom, N_c is the number of atoms in a primitive cell, and T_D is the high-temperature limit of the Debye temperature defined by

$$T_D^2 = \frac{5h^2\int_0^\infty \omega^2 D_p(\omega)\mathrm{d}\omega}{3k_B^2\int_0^\infty D_p(\omega)\mathrm{d}\omega}, \tag{18}$$

in which h is Planck's constant, ω is the frequency, and $D_p(\omega)$ is the phonon density of states (PDOS). $\langle\gamma^2\rangle$ is the mode-averaged square of the Grüneisen parameter given by

$$\langle\gamma^2\rangle = \frac{1}{C}\sum_{\mathbf{k}}\sum_{s=1}^{6} (\gamma_{s\mathbf{k}})^2 C_{s\mathbf{k}}, \tag{19}$$

where the Grüneisen parameter $\gamma_{s\mathbf{k}}$ for the sth mode of a given wave vector $\mathbf{k}$ is defined as

$$\gamma_{s\mathbf{k}} = -\frac{\partial \ln \omega_{s\mathbf{k}}}{\partial \ln V}, \tag{20}$$

where V is the volume per atom, $C_{s\mathbf{k}}$ is the phonon specific heat given by

$$C_{s\mathbf{k}} = k_B \frac{\left(\frac{\hbar\omega_{s\mathbf{k}}}{k_B T}\right)^2 e^{\hbar\omega_{s\mathbf{k}}/k_B T}}{(e^{\hbar\omega_{s\mathbf{k}}/k_B T} - 1)^2}, \tag{21}$$

and C is the total specific heat given by

$$C = \sum_{\mathbf{k}}\sum_{s=1}^{6} C_{s\mathbf{k}}. \tag{22}$$

Note that since the phonon frequencies $\omega_{s\mathbf{k}}(\mathbf{F},\boldsymbol{\xi})$ depend on the applied strain, thermodynamic properties such as T_D, γ, C, and k_b are all functions of strain. For the simplicity of notation, "$(\mathbf{F},\boldsymbol{\xi})$" is not shown explicitly for these quantities. After the bulk thermal conductivity k_b is obtained, the average phonon MFP can be calculated from approximated Kinetic theory by[31]

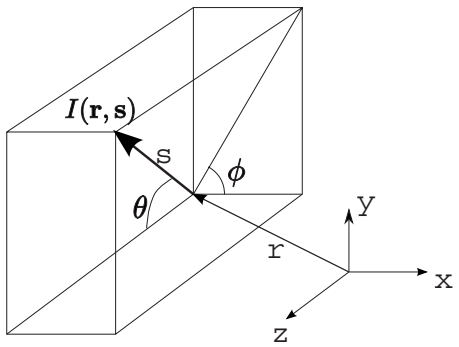

FIG. 4. Directional phonon intensity.

$$k_b \approx \frac{\Lambda}{3}\sum_{\mathbf{k}}\sum_{s=1}^{3} C_{s\mathbf{k}} v_{s\mathbf{k}} \quad s \in \text{acoustic phonon branches}, \tag{23}$$

where $v_{s\mathbf{k}}$ is the acoustic phonon group velocity given by

$$v_{s\mathbf{k}} = \left| \frac{\partial \omega_{s\mathbf{k}}}{\partial \mathbf{k}} \right|. \tag{24}$$

Note that in Eq. (23), only the acoustic branches of the phonon dispersion are included. The optical phonons are excluded for a better approximation of the average phonon MFP since they contribute little to the thermal conductivity around room temperature for Si and Ge due to their small group velocities. More detailed justification for this choice can be found in Refs. 32 and 31. The average phonon group velocity is then obtained from the average phonon MFP as

$$v = \frac{3k_b}{C^a \Lambda}, \tag{25}$$

where C^a is the acoustic phonon specific heat, which is obtained by summing $C_{s\mathbf{k}}$ over the acoustic branches. Again, the phonon scattering properties Λ and v are both functions of the strain.

C. BTE model for nanocomposites

Once the strain-dependent phonon thermal properties of the bulk Si and Ge are obtained, the effective thermal conductivity of nanocomposites can then be calculated by using a thermal transport model. Among various models that can be used to predict the thermal conductivity of nanocomposites,[19,33,34] BTE-based thermal modeling approaches have been developed and applied to thermal transport analysis in various applications with demonstrated accuracy and efficiency (see Ref. 22 for a review). In this work, we adopt the gray BTE approach for the computational thermal transport analysis of Si–Ge nanocomposites. The BTE model under gray assumption can be expressed in terms of total phonon intensity as[35,36]

$$\nabla \cdot [I(\mathbf{r},\mathbf{s}) \cdot \mathbf{s}] = -\frac{I(\mathbf{r},\mathbf{s}) - I_0(\mathbf{r})}{\Lambda}, \tag{26}$$

where $I(\mathbf{r},\mathbf{s})$ is the total phonon intensity at a spatial position $\mathbf{r}=\{x,y,z\}$ over a path length ds in the direction of unit vector $\mathbf{s}$. As shown in Fig. 4, $\mathbf{s}$ is defined by

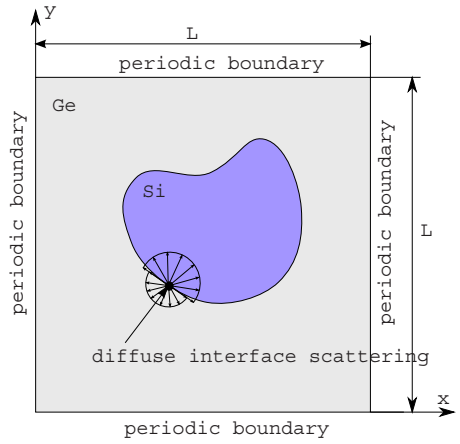

FIG. 5. (Color online) Unit cell of the nanocomposite material.

$$\mathbf{s} = \sin\theta\cos\phi\mathbf{e}_x + \sin\theta\sin\phi\mathbf{e}_y + \cos\theta\mathbf{e}_z, \tag{27}$$

where $\theta \in [0,\pi]$ and $\phi \in [0,2\pi]$ represent polar and azimuthal angles, respectively, and $\mathbf{e}_x$, $\mathbf{e}_y$, and $\mathbf{e}_z$ are the unit vectors in the x, y, and z directions, respectively. $I_0(\mathbf{r})$ is the equivalent equilibrium phonon intensity which is given by

$$I_0(\mathbf{r}) = \frac{1}{4\pi}\int_0^{2\pi}\int_0^{\pi} I(\mathbf{r},\mathbf{s})\sin\theta d\theta d\phi. \tag{28}$$

Assuming a uniform distribution of the Si nanowires, the BTE can be solved in a two-dimensional (2D) unit cell of the nanocomposite material as shown in Fig. 5. The edge length of the unit cell is denoted as L. The phonon intensities in the Si–Ge domains are determined by the BTE. Periodic boundary conditions are employed on the outer boundary of the unit cell. The phonon scattering at the Si–Ge interface is assumed to be diffuse. In this work, the boundary and interface models developed by Yang and Chen[13] for nanocomposites are adopted and implemented using the finite volume method (FVM). The boundary and interface conditions are briefly summarized as follows. For the top ($y=L$) and bottom ($y=0$) edges, the periodic boundary condition can be written as

$$I(x,L,\mathbf{s}) = I(x,0,\mathbf{s}), \tag{29}$$

for all x and $\mathbf{s}$. For the right ($x=0$) and left ($x=L$) edges, the periodic boundary condition implies that the difference between the phonon intensities in any given direction at the right and left edges is independent of y. This constant difference is imposed by a temperature drop ΔT between the left and right edges. The magnitude of ΔT, however, does not affect the result of the thermal conductivity. The periodic boundary condition is given by

$$I(0,y,\mathbf{s}) - I(L,y,\mathbf{s}) = \frac{v_{\mathrm{Ge}} C^a_{\mathrm{Ge}} \Delta T}{4\pi}, \tag{30}$$

where v_{Ge} and C^a_{Ge} denote the group velocity and acoustic specific heat of germanium, respectively. The diffuse interface scattering is represented by a simple diffuse mismatch model which assumes, at the interface, part of the phonons is transmitted through and the rest are reflected back. The transmitted and reflected phonons are evenly distributed across all

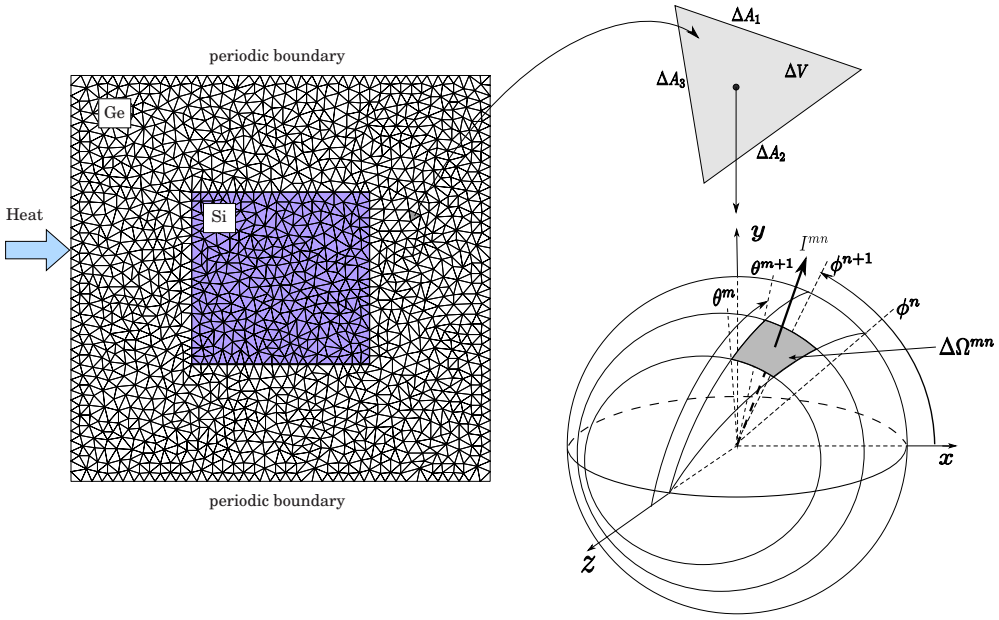

FIG. 6. (Color online) Spatial and angular discretization.

angles on each side of the interface, as shown in Fig. 5. From energy conservation, the relation of reflectivity R and transmissivity T is given by

$$T_{GS} = R_{SG} = 1 - T_{SG}, \tag{31}$$

where the subscript GS denotes from Ge into Si and vice versa, and T_{GS} is given by[31]

$$T_{GS} = \frac{C^a_{\mathrm{Si}} v_{\mathrm{Si}}}{C^a_{\mathrm{Ge}} v_{\mathrm{Ge}} + C^a_{\mathrm{Si}} v_{\mathrm{Si}}}. \tag{32}$$

By solving the BTE in both Si and Ge domains with the boundary and interface conditions, the phonon intensity $I(x,y,\mathbf{s})$ can be obtained. It is then straightforward to calculate the effective temperature distribution, heat flux, and thermal conductivity. Note that since the local thermal equilibrium condition breaks down in nanostructures, an effective temperature is used to represent the local energy density, i.e.,

$$T(x,y) = \frac{4\pi I_0(x,y)}{C^a v}. \tag{33}$$

The average temperature at each y-z plane along the x-direction is then obtained as

$$\bar{T}(x) = \frac{1}{L}\int_0^L T(x,y)\mathrm{d}y \tag{34}$$

The heat flux in the x-direction q_x is computed by integrating the x-component of the phonon intensity over the entire solid angle

$$q_x(x,y) = \int_0^{2\pi}\int_0^{\pi} I(x,y,\mathbf{s})\sin^2\theta\cos\phi d\theta d\phi. \tag{35}$$

The effective thermal conductivity is then calculated by using Fourier's law.

$$k_e = \frac{\int_0^L q_x(x,y)\mathrm{d}y}{\bar{T}(0) - \bar{T}(L)}. \tag{36}$$

Note that k_e is guaranteed to be constant along the x-axis by the periodic boundary condition imposed by Eq. (29).

D. Finite-volume solution of BTE

Due to the similarity between the thermal radiative transfer equation (RTE) and the BTE, numerical methods for solving RTE are often applicable to BTE. Among a variety of numerical methods that are used to solve the RTE, the discrete ordinates method (DOM) and the FVM are most popular. The DOM is known for its simplicity and efficiency. However, like the finite difference method, the DOM typically requires a structured grid, which imposes a major difficulty for problems involving complex geometries. In comparison, the FVM can be easily applied to unstructured meshes. Thus it provides greater flexibility in treating complex geometries. In addition, integration over the control angles is calculated exactly and heat flux in control volumes is automatically conserved in FVM.[37] Due to these attractive properties, the FVM has been employed for radiative thermal transport analysis in various applications.[38–41] It has also been applied to obtain BTE solution for heat transfer analysis of submicron structures.[42] In this work, as the Si–Ge nanocomposites to be investigated contain Si nanowires with different shaped cross sections as shown in Fig. 1, the FVM is employed in the computational analysis. One difficulty in the FVM solution of the BTE on an unstructured mesh is that the control angles may overlap with the control volume boundaries. In such cases, the overlapping control angle contains both the outgoing and incoming phonons. Several authors have addressed this issue for radiative heat transfer problems.[39,40,43] We employ an exact treatment proposed in Ref. 43. This treatment is found to be effective to resolve the problem for our calculations.

As shown in Fig. 6, the 2D domain of the Si–Ge unit cell is discretized into nonoverlapping triangular volumes (or elements). The volume of a given triangular element is denoted as ΔV. The length of the edges is denoted as ΔA_i, $i=1,2,3$. Within each triangular volume, the phonon intensity is defined on the center node of the triangular volume. The total solid angle 4π of the center node is discretized into $N_\theta \times N_\phi$ control angles along θ and ϕ directions. The control angles are denoted as $\Delta\Omega^{mn}$ $(1\leq m\leq N_\theta, 1\leq n\leq N_\phi)$, with the polar and azimuthal angles spanning from θ^m to θ^{m+1} and ϕ^n to ϕ^{n+1}, respectively, as shown in Fig. 6. Within each control volume and control angle $\Delta\Omega^{mn}$, the phonon intensity is assumed to be constant and denoted as I^{mn}. For each control volume and control angle, the governing BTE, Eq. (26), is integrated over ΔV and $\Delta\Omega^{mn}$ to yield

$$\int_{\Delta\Omega^{mn}}\int_{\Delta V}\nabla\cdot(I\mathbf{s})\mathrm{d}V\mathrm{d}\Omega=\int_{\Delta\Omega^{mn}}\int_{\Delta V}\left(-\frac{I-I_0}{\Lambda}\right)\mathrm{d}V\mathrm{d}\Omega. \tag{37}$$

Applying the divergence theorem, Eq. (37) can be rewritten as

$$\int_{\Delta\Omega^{mn}}\int_{\Delta A}I\mathbf{s}\cdot\mathbf{n}\mathrm{d}A\mathrm{d}\Omega=\int_{\Delta\Omega^{mn}}\int_{\Delta V}\left(-\frac{I-I_0}{\Lambda}\right)\mathrm{d}V\mathrm{d}\Omega. \tag{38}$$

For a given triangular control volume with a center node P, the phonon intensity in the control angle $\Delta\Omega^{mn}$ is denoted as I_P^{mn}. Assuming that for a given control angle, facial intensities are constant on each boundary face of the volume, the following finite-volume formulation can be obtained from Eq. (38) as

$$\sum_{i=1,2,3}I_i^{mn}\Delta A_i D_{Ci}^{mn}=\frac{1}{\Lambda}[-I_P^{mn}+(I_0^{mn})_P]\Delta V\Delta\Omega^{mn}, \tag{39}$$

where I_i^{mn} is the facial intensity on ΔA_i, $i=1,2,3$, and the directional weight D_{Ci}^{mn} is given by

$$D_{Ci}^{mn}=\int_{\theta^m}^{\theta^{m+1}}\int_{\phi^n}^{\phi^{n+1}}(\mathbf{s}\cdot\mathbf{n}_i)\sin\theta\mathrm{d}\theta\mathrm{d}\phi,\quad i=1,2,3, \tag{40}$$

where $\mathbf{s}$ is given by Eq. (27) and $\mathbf{n}_i$ is the outward normal of the ith face of the control volume. For 2D problems, D_{Ci}^{mn} can be obtained as

$$D_{Ci}^{mn}=\left[\frac{\Delta\theta}{2}-\frac{1}{4}(\sin 2\theta^{m+1}-\sin 2\theta^m)\right]\times[n_x(\sin\phi^{n+1}-\sin\phi^n)-n_y(\cos\phi^{n+1}-\cos\phi^n)], \tag{41}$$

where n_x and n_y are the x- and y-components of $\mathbf{n}_i$. In Eq. (40), the sign of D_{Ci}^{mn} (or equivalently, the sign of $\mathbf{s}\cdot\mathbf{n}_i$) determines whether the phonons are incoming or outgoing across the faces of control volume.

The facial intensity I_i^{mn} is then related to the nodal intensity by a step scheme assuming a downstream facial intensity is equal to the upstream nodal intensity. For example, as shown in Fig. 7, for face 2 of the control volume of node P, if the azimuthal angle of $\mathbf{s}$ is between ϕ^2 and ϕ^3, one obtains

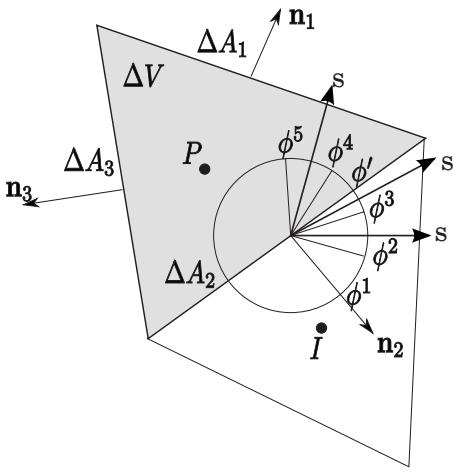

FIG. 7. Step scheme for the facial intensity.

$\mathbf{s}\cdot\mathbf{n}_2>0$, i.e., phonons are outgoing and P is the upstream node. Therefore, $I_{i=2}^{mn}=I_P^{mn}$. If $\mathbf{s}$ is between ϕ^4 and ϕ^5, then $\mathbf{s}\cdot\mathbf{n}_2<0$ and the node I of the neighbor control volume is the upstream node. Therefore, $I_{i=2}^{mn}=I_I^{mn}$. However, as shown in Fig. 7, the control angle from ϕ_3 to ϕ_4 overlaps with the face and contains both incoming and outgoing phonons. It is more involved to determine the facial intensity in this situation. The solution to this control angle overlap problem has been summarized in Ref. 39. In this work, we employ an exact treatment described in Ref. 43 which splits the control angle into $[\phi^3,\phi']$ and $[\phi',\phi^4]$ as shown in Fig. 7, and integrates the two resultant control angles separately. The facial intensity can be expressed by the following general expression as

$$I_i^{mn}D_{Ci}^{mn}=I_P^{mn}D_{Ci,\mathrm{out}}^{mn}+I_I^{mn}D_{Ci,\mathrm{in}}^{mn}, \tag{42}$$

where, for a nonoverlapping control angle,

if $\mathbf{s}\cdot\mathbf{n}_i>0$ then

$$D_{Ci,\mathrm{out}}^{mn}=\int_{\theta^m}^{\theta^{m+1}}\int_{\phi^n}^{\phi^{n+1}}(\mathbf{s}\cdot\mathbf{n}_i)\sin\theta\mathrm{d}\theta\mathrm{d}\phi,\quad D_{Ci,\mathrm{in}}^{mn}=0, \tag{43}$$

if $\mathbf{s}\cdot\mathbf{n}_i<0$ then

$$D_{Ci,\mathrm{in}}^{mn}=\int_{\theta^m}^{\theta^{m+1}}\int_{\phi^n}^{\phi^{n+1}}(\mathbf{s}\cdot\mathbf{n}_i)\sin\theta\mathrm{d}\theta\mathrm{d}\phi,\quad D_{Ci,\mathrm{out}}^{mn}=0, \tag{44}$$

For an overlapping control angle, without loss of generality, assuming $\mathbf{s}\cdot\mathbf{n}_i>0$ in $[\phi^n,\phi']$ and $\mathbf{s}\cdot\mathbf{n}_i<0$ in $[\phi',\phi^{n+1}]$, we have

$$D_{Ci,\mathrm{out}}^{mn}=\int_{\theta^m}^{\theta^{m+1}}\int_{\phi^n}^{\phi'}(\mathbf{s}\cdot\mathbf{n}_i)\sin\theta\mathrm{d}\theta\mathrm{d}\phi,$$

$$D_{Ci,\mathrm{in}}^{mn}=\int_{\theta^m}^{\theta^{m+1}}\int_{\phi'}^{\phi^{n+1}}(\mathbf{s}\cdot\mathbf{n}_i)\sin\theta\mathrm{d}\theta\mathrm{d}\phi. \tag{45}$$

When a control volume face is on the Si–Ge interface, the interface condition given in Eq. (31) is applied by replacing I_I^{mn} in Eq. (42) with

TABLE I. Room temperature thermodynamic properties of bulk Si.

C (J/m^3K)	T_D (K)	γ	v_{LA}^{Γ} (m/s)	v_{TA}^{Γ} (m/s)	v_{LA}^{X} (m/s)	k_b (W/mK)
1.59×10^6	720	0.79	8705	5470	4540	167.6
1.65×10^6 (Ref. 46)	645 (Ref. 47)	0.8 (Ref. 48)	8480 (Ref. 49)	5860 (Ref. 49)	4240 (Ref. 49)	156 (Ref. 50)

$$I_I^{mn} = \frac{R_{PI}}{\pi}\sum_{mn} I_P^{mn} D_{Ci,\text{out}}^{mn} - \frac{T_{IP}}{\pi}\sum_{mn} I_I^{mn} D_{Ci,\text{in}}^{mn}, \tag{46}$$

where R_{PI} is the reflectivity from medium of node P to the medium of node I and T_{IP} is the transmissivity from medium of node I to the medium of node P. It should be noted that the interface condition only modifies I_I^{mn} in Eq. (42) and I_P^{mn} remains the same. Otherwise, the transmission and reflection of the phonons would be double counted and the energy conservation condition would be violated. Substituting Eq. (42) into Eq. (39), the finite-volume formulation of the BTE for each control volume and control angle can be obtained as

$$\left[\sum_i \Delta A_i D_{Ci,\text{out}}^{mn} + \frac{\Delta V}{\Lambda}\Delta\Omega^{mn} - \frac{\Delta V}{4\pi\Lambda}(\Delta\Omega^{mn})^2\right] I_P^{mn} = -\sum_i \Delta A_i D_{Ci,in}^{mn} I_I^{mn} + \frac{\Delta V}{4\pi\Lambda}\left(\sum_{m'n'\neq mn} I_P^{m'n'}\Delta\Omega^{m'n'}\right)\Delta\Omega^{mn}. \tag{47}$$

For the global system, there are a total of $N_V\times N_\phi\times N_\theta$ equations, where N_V is the number of control volumes. These sets of equations are solved iteratively by using the Gauss–Seidel method. Note that, like the DOM, in Gauss–Seidel iterations, the nodal intensities are calculated in each control volume and control angle by using the values obtained from the last iteration. No global matrix storage is required. The iteration stops when the following convergence condition is reached,

$$\max[|I_P^{mn} - (I^{mn})_P^{old}|/I_P^{mn}] \leq 10^{-6}. \tag{48}$$

Note that while in this work we investigate the thermal conductivity of composite materials with periodic nanostructures, the approach presented is not limited to periodic systems. For nonperiodic systems, the analysis procedure remains the same with the periodic boundary conditions [Eqs. (29) and (30)] changing to temperature,[44] diffuse,[45] or other appropriate boundary conditions.

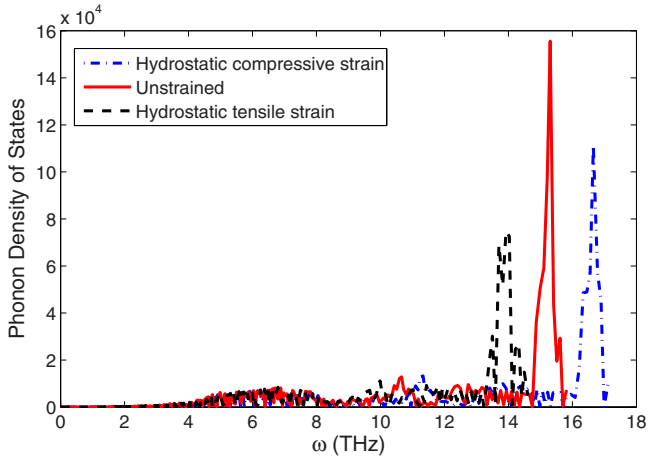

FIG. 8. (Color online) Strain-dependent phonon density of state of Si at T =300 K.

III. RESULTS AND DISCUSSION

A. Strain effect on thermodynamic properties of bulk Si and Ge

In this section, we investigate the strain effect on thermodynamic properties of bulk Si and Ge. From the lattice dynamics with Tersoff potential, various thermodynamic properties of bulk Si and Ge can be calculated. A few thermodynamic properties that are used in the calculation of the thermal conductivity are first calculated under unstrained condition. These results are compared with the experimental data and other theoretical results. Table I lists the specific heat (C), Debye temperature (T_D), Grüneisen parameter (γ), longitudinal acoustic (LA) group velocity at Γ point in the first Brillouin zone (v_{LA}^{Γ}), transverse acoustic group velocity at Γ point (v_{TA}^{Γ}), LA group velocity at X point (v_{LA}^{X}), and the bulk thermal conductivity (k_b) of silicon. The comparison shows that the Tersoff potential gives reasonable estimates to the thermodynamic properties, including the bulk thermal conductivity.

As mentioned in Sec. II A, we considered a maximum of 2% length change caused by four types of strains: hydrostatic compressive, hydrostatic tensile, uniaxial compressive, and uniaxial tensile. In the following discussion, if not otherwise specified, the strains correspond to a 2% length change, i.e., $F_{ii}=0.98$, $i=1,2,3$, and $F_{ij}=0$, $i\neq j$ for hydrostatic compressive strain, $F_{ii}=1.02$, $i=1,2,3$, and $F_{ij}=0$, $i\neq j$ for hydrostatic tensile strain, $F_{11}=0.98$, $F_{22}=F_{33}=1.0$, and $F_{ij}=0$, $i\neq j$ for uniaxial compressive strain, and $F_{11}=1.02$, $F_{22}=F_{33}=1.0$, and $F_{ij}=0$, $i\neq j$ for uniaxial tensile strain.

Figure 8 shows the strain effect on the PDOS of Si under hydrostatic compressive and tensile strains. A direct sampling method is used in the calculation of PDOS, which generates $100\times100\times100$ uniformly distributed $\mathbf{k}$-points in the first Brillouin zone and approximates the PDOS by a normalized histogram. It is shown that a shift in optical phonons to the left occurs when the tensile strain is applied, while a shift to the right occurs for the compressive strain. In other words, compared to the unstrained case, most optical phonons will be at a lower (or higher) energy when tensile (or compressive) strain is applied. Note that there are similar peak shifts for LA phonons, indicating that the hydrostatic strain has a significant effect on them as well. Variations in transverse acoustic phonons are also observed, although not equally significant compared to the LA and optical phonons. Similar

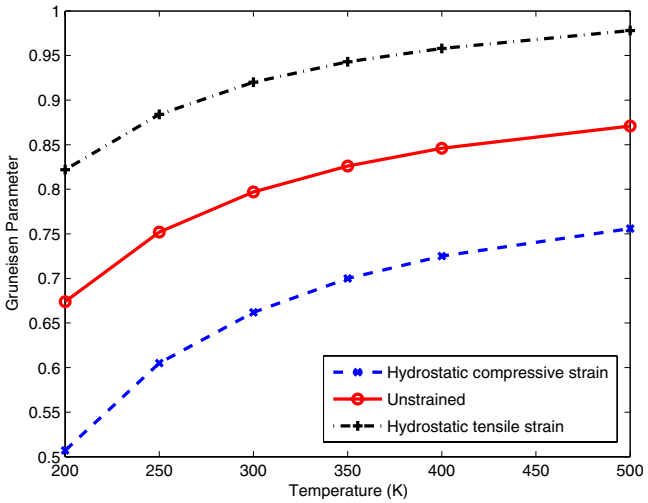

FIG. 9. (Color online) Strain-dependent Grüneisen parameter of Si with respect to temperature.

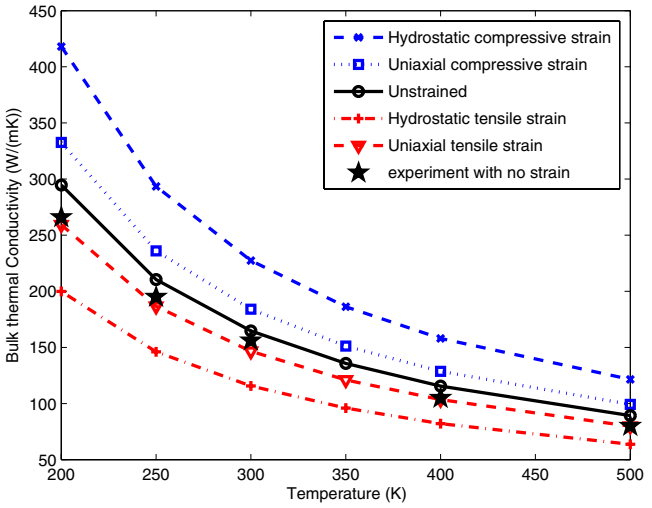

FIG. 11. (Color online) Strain-dependent bulk thermal conductivity of Si between 200 and 500 K.

behavior of the PDOS is observed for Ge under strain (not shown). The different frequency shift direction of the PDOS is largely due to the change in the stiffness of the atomic bonds, which is represented by the force constants given in Eq. (14), i.e., a compressive (tensile) strain increases (decreases) the force constants and consequently increases (decreases) the vibration frequencies of the atoms. Figure 9 shows the overall Grüneisen parameter under hydrostatic strain at different temperatures. It is shown that Grüneisen parameter increases when temperature increases and when tensile strain is applied. Again, similar behavior of the Grüneisen parameter of Ge is observed.

Figure 10 shows the Debye temperature of bulk Si crystal under hydrostatic compressive, uniaxial compressive, hydrostatic tensile and uniaxial tensile strains at the temperature range 200–500 K comparing to the results of the unstrained case. The Debye temperature is almost independent of temperature but shows a strong dependence on strains. Debye temperature's increase with compressive strains and its decrease with the tensile strains can be explained from the PDOS variation shown in Fig. 8. In addition, it is shown in the figure that with the same 2% length change, hydrostatic strains produce a larger effect on T_D than the uniaxial strains.

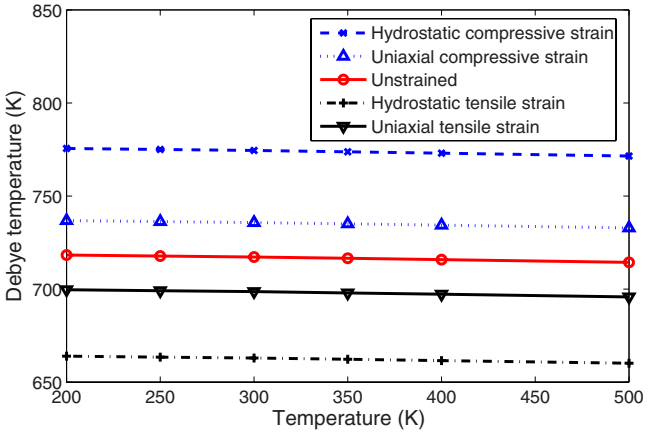

FIG. 10. (Color online) Strain-dependent Debye temperature of Si between 200 and 500 K.

With the decrease in Grüneisen parameter and the increase in Debye temperature for compressive strains, the Slack relation given in Eq. (17) predicts an increase in bulk phonon thermal conductivity. Similarly, a reduction in thermal conductivity is predicted for tensile strains. The same conclusions can be obtained for Ge. Figure 11 shows the bulk thermal conductivity of Si with respect to temperature and strain. In Ref. 29, Slack has qualitatively explored the strain effect on bulk thermal conductivity of crystalline solids by assuming possible changes in Debye temperature and Grüneisen parameter due to strain. Our calculations have confirmed his prediction quantitatively. Figure 11 shows that hydrostatic strains have a stronger effect on bulk thermal conductivity than the uniaxial strains. The stars in the figure show the experiment data of unstrained bulk Silicon taken from Table I of Ref. 50. The calculated unstrained bulk thermal conductivities are higher than experiment results but in reasonable agreement.

Figure 12 shows the contribution of optical phonons to the overall specific heat. It is shown that, at low temperatures ($T<100$ K), acoustic phonons are the major contributors to specific heat but at high temperatures ($T>400$ K), optical phonons contribute about half of the total specific heat. Simi-

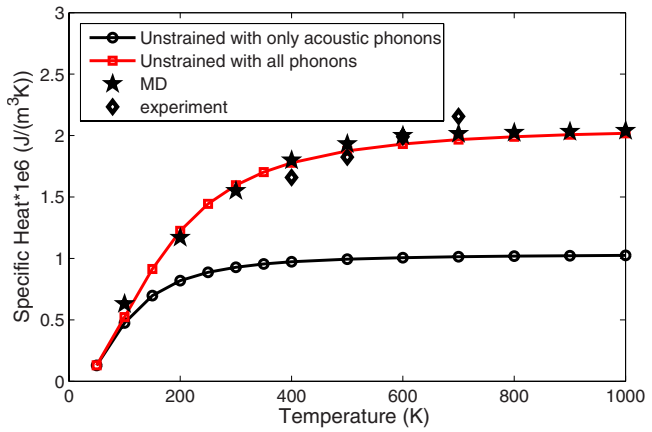

FIG. 12. (Color online) Specific heat of Si.

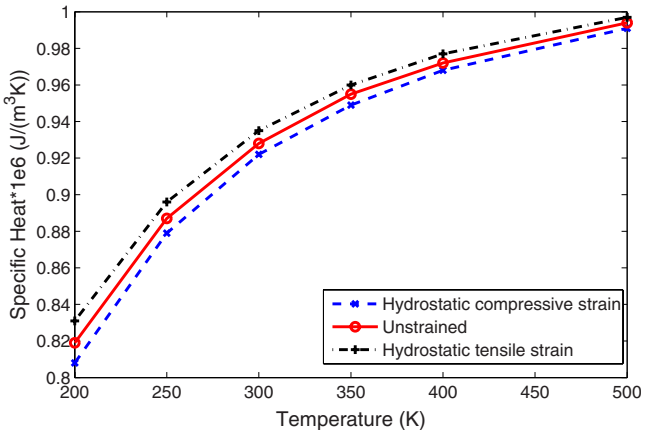

FIG. 13. (Color online) Strain-dependent acoustic specific heat of Si between 200 and 500 K.

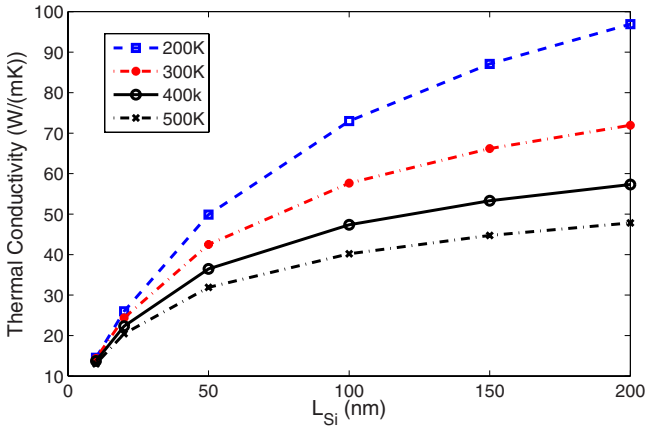

FIG. 15. (Color online) Thermal conductivity of nanocomposites with respect to temperature (square Si nanowire cross section).

lar results have been obtained in Ref. 31. Since the optical phonons contribute little to heat transfer due to their small group velocities, it is justifiable to exclude the optical phonons in the calculation of the phonon MFP and average group velocity as shown in Eqs. (23) and (25). MD data taken from Fig. 10 of Ref. 27 and experiment data taken from Fig. 1 of Ref. 51 are also shown in Fig. 12. The strain and temperature-dependence of the acoustic specific heat is shown in Fig. 13, where a compressive strain decreases the specific heat and a tensile strain increases it. Once again, the results for Ge are similar. The results are not shown for the sake of brevity.

Figure 14 shows the variation in average group velocity with respect to strain-induced length change. For the small strains considered here, the group velocity shows a nearly linear dependence on the length change, for both hydrostatic and uniaxial cases. For the same length change, hydrostatic strain leads to a larger variation than uniaxial strain. The group velocities of unstrained Si and Ge at room temperature are calculated to be 3138 and 2233 m/s, respectively. In Ref. 13, the group velocities of Si and Ge were calculated by approximating the phonon dispersion using a simple sine function. The results are 1804 m/s for Si and 1042 m/s for Ge. It should be noted that this discrepancy is largely due to the differences in the phonon dispersion and the PDOS given by the Tersoff potential and the sine function.

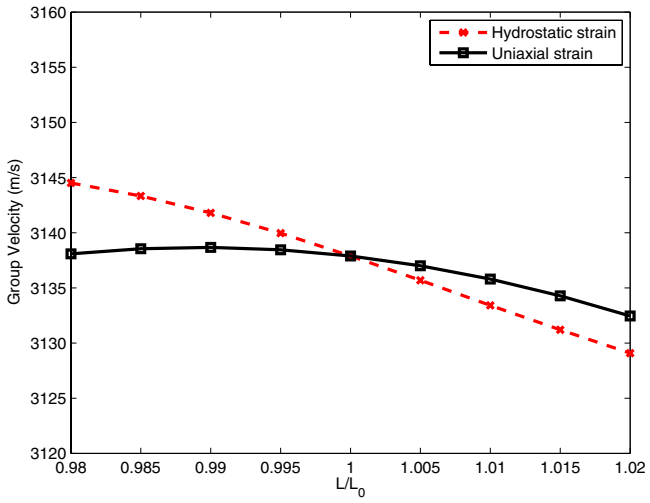

FIG. 14. (Color online) Average group velocity of Si as a function of strain-induced length change (L_0 is the undeformed length).

B. Strain-dependent thermal conductivity of nanocomposites

Having calculated the thermal properties of bulk Si and Ge as functions of strain, the effective thermal conductivity is computed for the Si–Ge nanocomposites shown in Fig. 1 by using the FVM and solving the BTE over unstructured triangle meshes as shown in Fig. 6. The atomic percentage of Si is fixed at 20%, i.e., the nanocomposites are all $Si_{0.2}Ge_{0.8}$. In all calculations, θ is discretized uniformly into 12 angles from 0 to π, while ϕ is discretized into 24 angles from 0 to 2π.

Figure 15 shows the size and temperature effects on phonon thermal conductivity of the $Si_{0.2}Ge_{0.8}$ nanocomposite with square cross section Si nanowires. The x-coordinate is the characteristic length of the Si nanowire, denoted as L_{Si}, which is the width of the square cross section. Thermal conductivity of the nanocomposite decreases when the temperature increases or when size decreases. The large reduction in the thermal conductivity with the decreasing characteristic length is due to the dominance of the interface scattering over the ballistic transport in nanocomposites.[13] Figure 15 shows that this interface scattering induced thermal conductivity reduction holds over a wide range of temperatures while the effect is more significant at low temperatures.

The heat flux in the x-direction of the unstrained $Si_{0.2}Ge_{0.8}$ nanocomposite with 10×10 nm^2 Si nanowire at $T=300$ K is shown in Fig. 16. The low heat flux along the path blocked by the Si wire is clearly due to the phonon scattering at the Si–Ge interface. The effect of strain along with the size effect on the effective thermal conductivity is shown in Figs. 17 and 18. It is shown that strain has a significant effect on the thermal conductivity of the nanocomposite. Depending on the characteristic length of the silicon nanowire, with a length change of 2%, an applied hydrostatic tensile or compressive strain can reduce or increase the thermal conductivity up to 22%, while uniaxial tensile or compressive strain can reduce or increase the thermal conductivity by as much as 8%. More importantly, the strain effect on

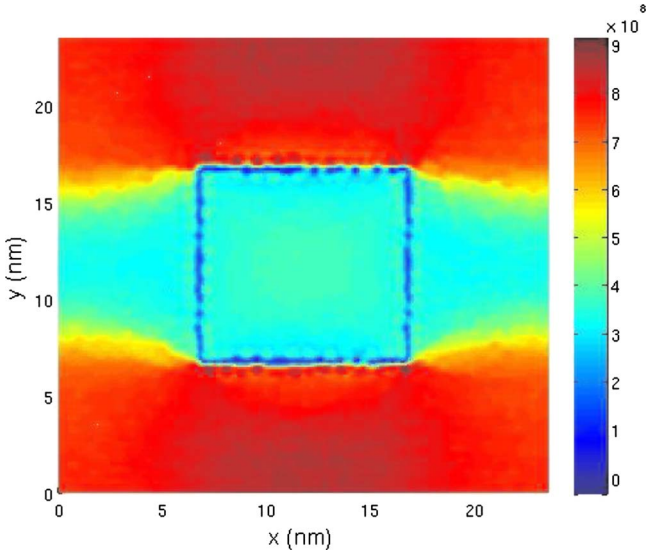

FIG. 16. (Color online) Heat flux profile of unstrained $Si_{0.2}Ge_{0.8}$ at 300 K (Si nanowire with 10×10 nm^2 square cross section).

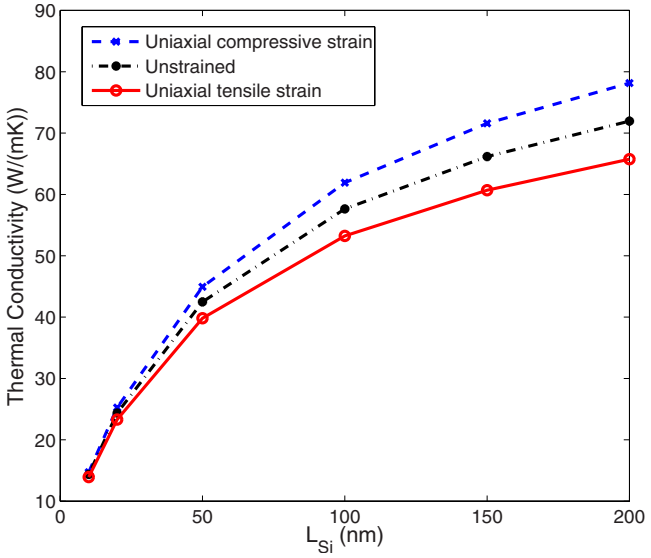

FIG. 18. (Color online) Thermal conductivity of $Si_{0.2}Ge_{0.8}$ under uniaxial strain at 300 K (square Si nanowire cross section).

the thermal conductivity of bulk materials is largely preserved in the composite configuration over all the sizes. This result shows that the mechanical effect can be combined with structural effects such as size and composition effects to further manipulate and control the thermal conductivity of nanomaterials and nanostructures.

Another structural aspect to explore in this work is the effect of the cross-sectional shape of the Si nanowire. Keeping the atomic percentage of the Si nanowire at 20%, we change the cross-sectional shape of the Si nanowire to be circular and diamond-shaped. Note that, for circular cross sections, the characteristic length L_{Si} is the diameter. For diamond cross sections, the characteristic length L_{Si} is the length of the edges. Same set of calculations are performed to obtain the strain and size effects on the effective thermal conductivity. The heat flux profiles for the circular and diamond-shaped cross sections are shown in Figs. 19 and 20. The difference in the heat flux profiles is obvious, especially the shape of the low heat flux regions (the light colored regions). However, it is observed that the curves of the effective thermal conductivity are very similar to those shown in Figs. 17 and 18, except at the lower limit of the characteristic length. Figure 21 shows the thermal conductivities for the three types of Si nanowires at the characteristic length of 10 nm under hydrostatic strains at 300 K. The strain effect is almost the same for the three nanocomposites. The circular and square cases have very close thermal conductivities, with or without strain. The magnitude of the thermal conductivity for diamond-shaped cross section is appreciably lower (about 5%). Figure 22 shows the difference in thermal conductivity for diamond and square cross sections over the characteristic length from 10 to 200 nm. The thermal conductivity difference between the two nanocomposites drops exponentially. These results show that, with the same atomic percentage of Si, the cross-sectional shape makes little difference when the

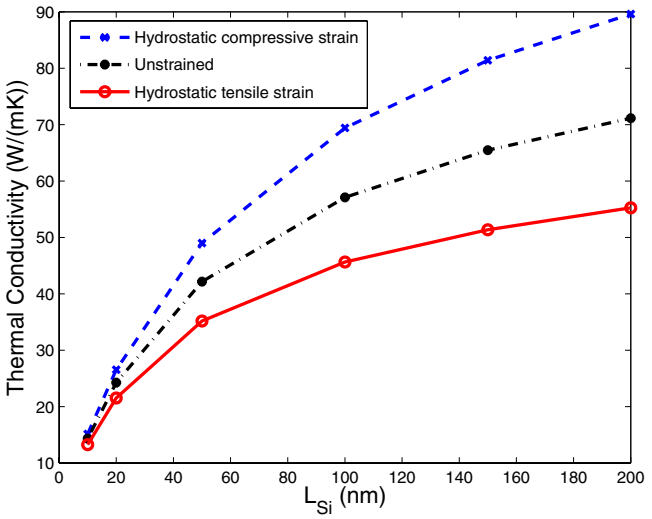

FIG. 17. (Color online) Thermal conductivity of $Si_{0.2}Ge_{0.8}$ under hydrostatic strain at 300 K (square Si nanowire cross section).

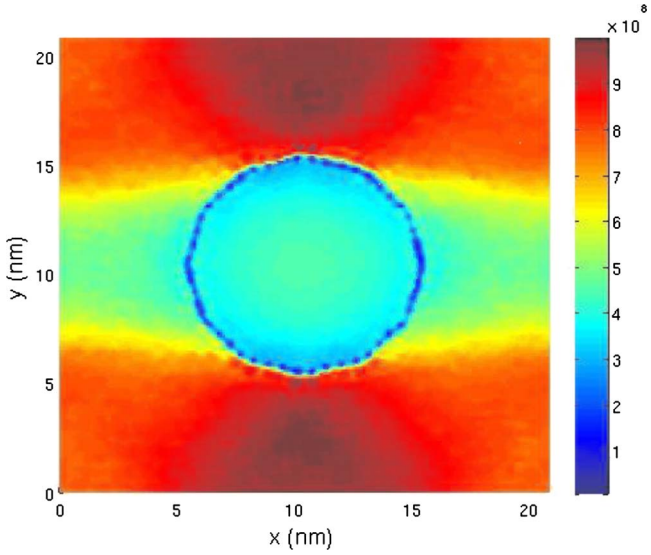

FIG. 19. (Color online) Heat flux profile of unstrained $Si_{0.2}Ge_{0.8}$ at 300 K (circular Si nanowire cross section with the characteristic length of 10 nm).

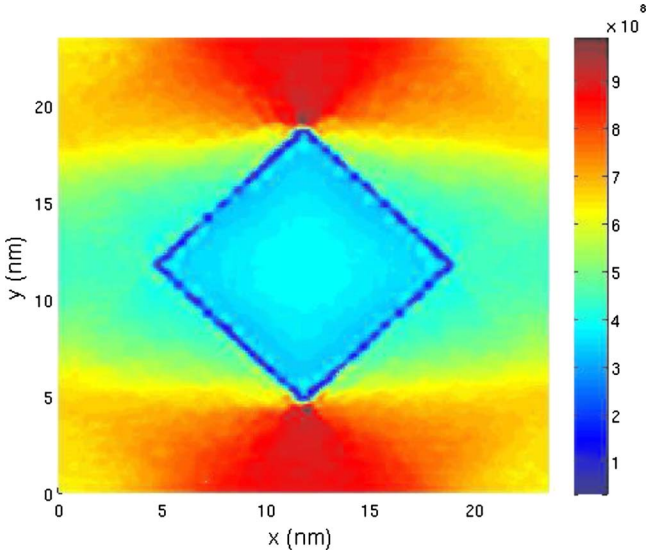

FIG. 20. (Color online) Heat flux profile of unstrained $Si_{0.2}Ge_{0.8}$ at 300 K (diamond-shaped Si nanowire cross section with the characteristic length of 10 nm).

characteristic length increases. However, for very small systems (e.g., characteristic length <10 nm), the cross-sectional shape starts to play a role.

IV. CONCLUSIONS

A modeling and analysis approach to investigate the strain effect on the thermal transport in 2D Si–Ge nanocomposites has been developed in this paper. Strains are incorporated into the lattice dynamics by using the Cauchy–Born rule. Thermal properties calculated from strain-dependent lattice dynamics are then used in the phonon BTE for the thermal transport analysis of nanocomposites. A FVM is employed to solve the BTE over unstructured meshes. Our results show that the phonon thermal conductivity of the nanocomposites can be significantly decreased (or increased) by a tensile (or compressive) strain. With the same length change, hydrostatic strain produces a larger variation in phonon thermal conductivity than uniaxial strain. Depending on the size and shape of the embedded silicon nanowire, a hydrostatic tensile strain corresponding to a length change of 2% can reduce the thermal conductivity of $Si_{0.2}Ge_{0.8}$ by as much as 22%, while a uniaxial tensile strain of 2% length change gives a maximum reduction of 8%. The shape effect on the thermal conductivity is also studied, it is found that with the same atomistic percentage, the cross-sectional shape makes little difference to the effective thermal conductivity except at very small characteristic lengths.

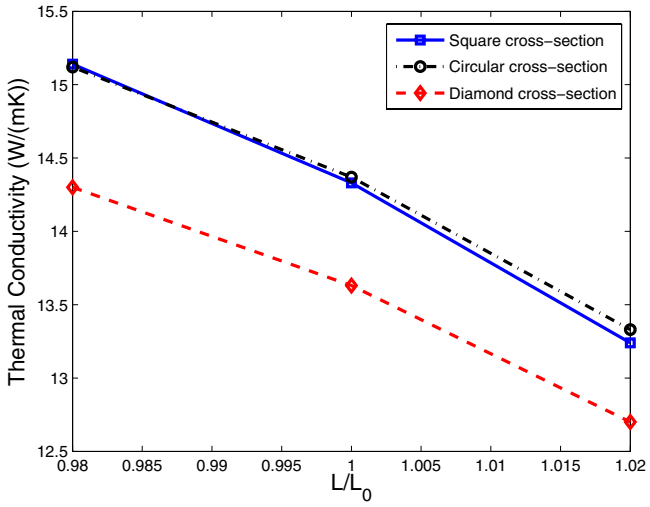

FIG. 21. (Color online) Thermal conductivity of $Si_{0.2}Ge_{0.8}$ with different cross section shapes of Si nanowire under hydrostatic strains at 300 K.

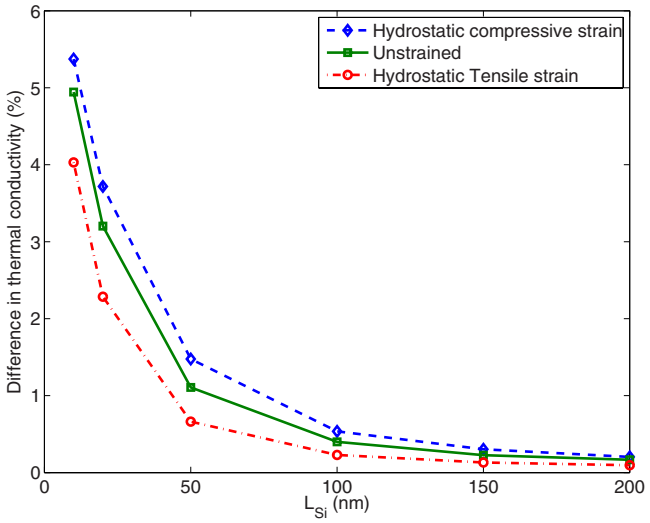

FIG. 22. (Color online) Difference in thermal conductivity between diamond-shaped and square cross sections as a function of characteristic length.

ACKNOWLEDGMENTS

We gratefully acknowledge support by the National Science Foundation under Grant No. CMMI-0800474 and the Clemson University start-up funds.

[1] Y. Xia, P. Yang, Y. Sun, Y. Wu, B. Mayers, B. Gates, Y. Yin, F. Kim, and H. Yan, Adv. Mater. **15**, 353 (2003).
[2] A. S. Arico, P. Bruce, B. Scrosati, J. M. Tarascon, and W. V. Schalkwijk, Nature Mater. **4**, 366 (2005).
[3] R. J. Gehr and R. W. Boyd, Chem. Mater. **8**, 1807 (1996).
[4] P. T. Hammond, Adv. Mater. **16**, 1271 (2004).
[5] M. S. Dresselhaus, G. Chen, M. Y. Tang, R. Yang, H. Lee, D. Wang, Z. Ren, J.-P. Fleurial, and P. Gogna, Adv. Mater. **19**, 1043 (2007).
[6] H. J. Goldsmid, *Thermoelectric Refrigeration* (Plenum, New York, 1964).
[7] R. Venkatasubramanian, Semicond. Semimetals **71**, 175 (2001).
[8] G. Chen and A. Shakouri, ASME J. Heat Transfer **124**, 242 (2002).
[9] R. Venkatasubramanian, E. Siivola, T. Colpitts, and B. O'Quinn, Nature (London) **413**, 597 (2001).
[10] B. Zhang, J. He, X. Ji, and T. M. Tritt, Appl. Phys. Lett. **89**, 163114 (2006).
[11] K. M. Lee, T. Weissgarber, and B. Kieback, J. Mater. Sci. **39**, 5235 (2004).
[12] Y. Yang, M. C. Gupta, J. N. Zalameda, and W. P. Winfree, Micro & Nano Lett. **3**, 35 (2008).
[13] R. Yang and G. Chen, Phys. Rev. B **69**, 195316 (2004).
[14] R. W. Keyes and R. J. Sladek, Phys. Rev. **125**, 478 (1962).
[15] L. J. Challis and S. C. Haseler, J. Phys. C **11**, 4681 (1978).
[16] A. Ramdane, B. Salce, and L. J. Challis, Phys. Rev. B **27**, 2554 (1983).
[17] K. C. Sood and M. K. Roy, Phys. Rev. B **46**, 7486 (1992).
[18] T. Borca-Tasciuc, W. Liu, J. Liu, T. Zeng, D. W. Song, C. D. Moore, G. Chen, K. L. Wang, M. S. Goorsky, T. Radetic, R. Gronsky, T. Koga, and M. S. Dresselhaus, Superlattices Microstruct. **28**, 199 (2000).
[19] A. R. Abramson, C. L. Tien, and A. Majumdar, ASME J. Heat Transfer **124**, 963 (2002).

[20]R. C. Picu, T. Borca-Tasciuc, and M. C. Pavel, J. Appl. Phys. **93**, 3535 (2003).
[21]J. M. Ziman, *Electrons and Phonons* (Clarendon, Oxford, 1960).
[22]S. V. J. Narumanchi, J. Y. Murthy, and C. H. Amon, Heat Mass Transfer **42**, 478 (2006).
[23]J. Tersoff, Phys. Rev. B **38**, 9902 (1988).
[24]D. W. Brenner, Phys. Rev. B **42**, 9458 (1990).
[25]F. H. Stillinger and T. A. Weber, Phys. Rev. B **31**, 5262 (1985).
[26]J. Tersoff, Phys. Rev. B **39**, 5566 (1989).
[27]H. Zhao, Z. Tang, G. Li, and N. R. Aluru, J. Appl. Phys. **99**, 064314 (2006).
[28]M. Born and K. Huang, *Dynamical Theory of Crystal Lattices* (Clarendon, Oxford, 1954).
[29]G. A. Slack, Solid State Phys. **34**, 1 (1979).
[30]B. L. Huang and M. Kavianya, J. Appl. Phys. **100**, 123507 (2006).
[31]G. Chen, Phys. Rev. B **57**, 14958 (1998).
[32]G. Chen, ASME J. Heat Transfer **119**, 220 (1997).
[33]D. A. Broido, M. Malorny, G. Birner, N. Mingo, and D. A. Stewart, Appl. Phys. Lett. **91**, 231922 (2007).
[34]W. Zhang, T. S. Fisher, and N. Mingo, Numer. Heat Transfer, Part B **51**, 333 (2007).
[35]A. Majumdar, ASME J. Heat Transfer **115**, 7 (1993).
[36]G. Chen, ASME J. Heat Transfer **118**, 539 (1996).
[37]G. D. Raithby, Numer. Heat Transfer, Part B **35**, 389 (1999).
[38]E. H. Chui, G. D. Raithby, and P. M. J. Hughes, J. Thermophys. Heat Transfer **6**, 605 (1992).
[39]M. Y. Kim, S. W. Baek, and J. H. Park, Numer. Heat Transfer, Part B **39**, 617 (2001).
[40]J. Y. Murthy and S. R. Mathur, J. Thermophys. Heat Transfer **12**, 313 (1998).
[41]J. C. Chai, H. S. Lee, and S. V. Patankar, J. Thermophys. Heat Transfer **8**, 419 (1994).
[42]S. V. J. Narumanchi, J. Y. Murthy, and C. H. Amon, ASME J. Heat Transfer **126**, 946 (2004).
[43]S. W. Baek, M. Y. Kim, and J. S. Kim, Numer. Heat Transfer, Part B **34**, 419 (1998).
[44]D. Baillis and J. Randrianalisoa, Int. J. Heat Mass Transfer **52**, 2516 (2009).
[45]J. Zou and A. Balandin, J. Appl. Phys. **89**, 2932 (2001).
[46]P. Flubacher, A. J. Leadbetter, and J. A. Morrison, Philos. Mag. **4**, 273 (1959).
[47]C. Kittel, *Introduction to Solid State Physics* (Wiley, New York, 1995).
[48]L. J. Porter, S. Yip, M. Yamaguchi, H. Kaburaki, and M. Tang, J. Appl. Phys. **81**, 96 (1997).
[49]P. Chantrenne, J. L. Barrat, X. Blase, and J. D. Gale, J. Appl. Phys. **97**, 104318 (2005).
[50]C. J. Glassbrenner and G. A. Slack, Phys. Rev. **134**, A1058 (1964).
[51]V. M. Glazov, A. S. Pashinkin, and M. S. Mikhailova, Scand. J. Metall. **30**, 388 (2001).